# Beyond Channel Count: Metrological Performance Metrics for Compact Multi-Channel Spectral Sensors

Alberto Besozzi, Giovanni Gibertoni, Luigi Rovati, Agostino Gibaldi
University of Modena and Reggio Emilia, Via Pietro Vivarelli, 10, Modena, Italy

## ABSTRACT

Compact multi-channel spectral sensors based on thin-film interference filters offer a low-cost, integrable alternative to dispersive spectrometers, yet their performance is too often assessed by channel count alone, an indicator blind to inter-channel crosstalk, filter bandwidth, and the underdetermined nature of the spectral measurement. We present a metrological framework that formalises the channel-wise measurement model, identifies the dominant Type B instrumental uncertainty contributions (interference-filter centre-wavelength tolerance, responsivity line-shape deviation, PGA gain tolerance, and ADC quantisation and noise), and propagates them from the digital-count domain to irradiance through the device calibration curve. From the same datasheet parameters, the framework derives two figures of merit: the inter-channel crosstalk matrix $\mathbf{C}$ and the effective number of independent measurements $M_{\text{eff}}$, obtained as the participation ratio of the eigenvalues of $\mathbf{C}$. The uncertainty budget is developed in detail for the AS7343, a device with broad and overlapping filters, under three calibration scenarios of increasing effort, while the figures of merit are computed for both the AS7341 and the AS7343. Predictions are cross-validated against the experimental spectral reconstruction errors reported in our previous calibration study on xenon illuminants. Although the AS7343 carries three more nominal channels than the AS7341, the two devices share an almost identical effective channel count ($M_{\text{eff}} = 7.05$ versus 7.07) and reconstruct the xenon test source comparably, demonstrating that channel count is a poor predictor of metrological quality and that the proposed metrics offer a predictive, datasheet-level basis for sensor characterisation and selection.

**Keywords:** multi-channel spectral sensor, interference filter, crosstalk, measurement uncertainty, effective degrees of freedom, spectral resolution, spectral reconstruction

## 1. INTRODUCTION

Spectral measurement underpins a wide range of disciplines, from food and pharmaceutical quality assessment to remote sensing, biomedical diagnostics, smart agriculture, and lighting control.[1–6] Historically, this need has been served by dispersive spectrometers, which employ a diffraction grating or a prism to project the spectrum onto a linear detector array, providing continuous sampling up to sub-nanometre resolution.[7,8] While metrologically powerful, such instruments remain expensive, mechanically delicate, and complex to use, limiting their adoption in embedded, mobile, or distributed sensing systems. To overcome these limitations, compact multi-channel spectral sensors have emerged over the last decade as a viable low-cost alternative.[9] These devices integrate, on a single CMOS die, an array of photodiodes each covered by a thin-film interference filter centred on a different wavelength.[10,11] The resulting monolithic integration of the optical-filtering and photodetection functions removes the need for any moving or dispersive element, enabling devices that occupy a few square millimetres, consume a few milliwatts, and communicate via standard digital interfaces like I$^2$C. Typical commercial devices contain between 3 and 14 channels spanning the visible and near-infrared range. Their compactness has enabled adoption in a growing range of applications.

The measurement performed by these sensors is, however, fundamentally different from that of a dispersive instrument. Classical spectrometers sample the spectral power distribution $S(\lambda)$ according to the Nyquist criterion, achieving a resolution on the order of 1–3 nm. These multi-channel sensors, on the other hand, rely on a very small number of channels with broader Gaussian-shaped responsivities. As a result, recovering $S(\lambda)$ from the channel readings is an underdetermined inverse problem, and the quality of the reconstruction depends strongly

Send correspondence to A.B.: alberto.besozzi@unimore.it, Tel.: +39 331 4877702

on the spectral placement and bandwidth of each channel. A sensor with broad, overlapping filters effectively measures fewer distinct spectral features than its nominal count would suggest, and two devices with the same number of channels may differ substantially in their reconstruction capabilities. For these reasons, a more rigorous, design-level characterisation is needed both to compare sensors fairly and to predict their behaviour in real applications. In our previous work,[12] we addressed part of this gap by introducing a calibration framework for three commercial multi-channel sensors (AS7262, AS7341, AS7343), to assess the absolute optical power reaching each channel. The framework demonstrated quantitatively that reconstruction errors vary significantly across sensors and across source types, with devices having broader or more overlapping channels performing markedly worse on sources featuring narrower spectral peaks.

In the present work, we perform a metrological evaluation of these compact spectral sensors. We first identify the instrumental uncertainty contributions and develop the resulting budget in detail for the AS7343. We then introduce two figures of merit, computed for AS7341 and AS7343 directly from the device specifications: (i) the inter-channel crosstalk matrix $\mathbf{C}$, and (ii) the effective number of independent measurements $M_{\text{eff}}$. We apply this framework to the AS7341 and AS7343 sensors and compare the resulting characterisation with the experimental reconstruction errors reported in Besozzi et al.[12]

# 2. METHODS

## 2.1 Measurement model

Each sensor consists of $M$ channels and implements a linear operator $\mathcal{L} : L^2(\Lambda) \to \mathbb{R}^M$, which projects the continuous SPD $S(\lambda)$ onto an $M$-dimensional subspace spanned by the channel responsivities $\{\hat{R}_i(\lambda)\}_{i=1}^{M}$. The reading of the $i$-th channel is given by

$$y_i = \int_{\lambda_{\min}}^{\lambda_{\max}} S(\lambda)\, \hat{R}_i(\lambda)\, d\lambda \quad \text{counts}, \tag{1}$$

where $\Lambda = [\lambda_{\min}, \lambda_{\max}] = [380, 780]\,\text{nm}$. Discretising this range on a uniform grid of $N \gg M$ points, Eq. (1) can be rewritten as the linear system

$$\mathbf{y} = \mathbf{A}\,\mathbf{s}, \qquad \mathbf{A} \in \mathbb{R}^{M\times N}, \tag{2}$$

where the rows of the measurement matrix $\mathbf{A}$ correspond to the sampled responsivities $\hat{R}_i(\lambda)$, normalised to unit peak, but since $M \ll N$, recovering $\mathbf{s}$ from $\mathbf{y}$ is a severely underdetermined inverse problem. The responsivity of each channel is determined by the thin-film interference bandpass filters used, which are well approximated by a Gaussian profile, with deviations on side-band typically suppressed below $-30\,\text{dB}$, and slightly different peak wavelength. Accordingly, the normalised responsivity of the $i$-th channel is written as

$$\hat{R}_i(\lambda) = \exp\left[-\frac{(\lambda - \lambda_i)^2}{2\sigma_i^2}\right], \qquad \sigma_i = \frac{w_i}{2\sqrt{2\ln 2}}, \tag{3}$$

where $\lambda_i$ denotes the centre wavelength and $w_i$ the FWHM, both taken from the device datasheet. Equation (3) provides the building block for the inner products used throughout the rest of this section.

### 2.1.1 Calibration models

The relation between the digital reading $y_i$ and the absolute irradiance $E_i$, established by the calibration procedure performed in Besozzi et al., is well described by a quadratic law of the form

$$y_i = a_i\, E_i^2 + b_i\, E_i, \tag{4}$$

where the coefficients $\{a_i, b_i\}$ are channel-specific and depend on the chosen integration time $t_{\text{int}}$ and PGA gain $G$. Equation (4) passes through the origin by construction, since a null irradiance produces a null reading once the dark offset has been subtracted. The full-scale irradiance $E_{\text{FS},i}$ of the channel is defined as the irradiance that drives the reading to the maximum ADC value $y_{\text{FS}} = 65535$, since the ADC has $n_b = 16$ bits resolution; solving Eq. (4) for $E_i$ at $y_i = y_{\text{FS}}$ yields

$$E_{\text{FS},i} = \frac{-b_i + \sqrt{b_i^2 + 4\, a_i\, y_{\text{FS}}}}{2\, a_i} \quad \mu W/cm^2 \tag{5}$$

Since $\{a_i, b_i\}$ depend on $t_{\text{int}}$ and $G$, the full-scale irradiance $E_{\text{FS},i}$ is itself a function of the chosen acquisition settings: a longer integration time or a higher gain reduces $E_{\text{FS},i}$, as the reading saturates at a lower irradiance. For this reason, the uncertainty budget developed below is expressed in general terms, independent of this specific source of variability.

## 2.2 Type B instrumental uncertainty sources

In Figure 1, the acquisition chain is shown, from light hitting the device, through internal electronics to digital output. Each stage introduces an uncertainty on the channel reading and, ultimately, on the retrieved irradiance. Following the GUM recommendations,[13] all contributions identified in this work belong to Type B and they are computed from data documented in the device datasheets. The uncertainty budget is developed in detail for the AS7343, the device with the broadest and most overlapping filters; the same procedure applies, channel by channel, to the other two sensors.

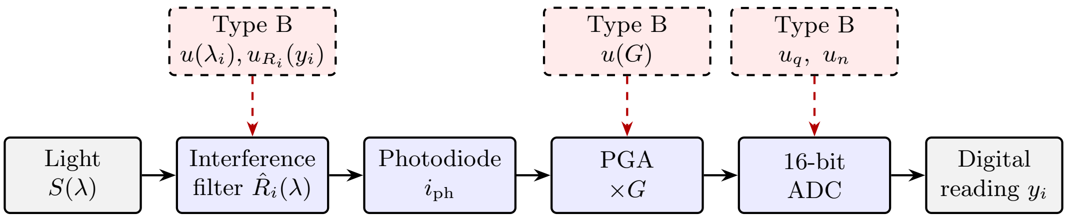


Figure 1. Acquisition chain of a compact multi-channel spectral sensor and associated Type B uncertainty contributions. The interference filter introduces a centre-wavelength tolerance $u(\lambda_i)$ and a responsivity deviation $u_{R_i}(y_i)$; the programmable-gain amplifier (PGA) applies a tolerance-limited multiplicative factor $G$ with standard uncertainty $u(G)$; the 16-bit ADC contributes both a quantisation term $u_q$ and an intrinsic noise term $u_n$ specified by the manufacturer.

### 2.2.1 Interference filter uncertainty

The thin-film deposition process used for interference filters introduces a finite tolerance on the peak transmission wavelength. The datasheets of the AS7341 and AS7343 specify a deviation of $\Delta\lambda = \pm 10\,\text{nm}$ with respect to the nominal centre wavelength $\lambda_i$. In the absence of further information on its distribution, a rectangular probability density function is assumed over the declared interval, yielding the standard uncertainty

$$u(\lambda_i) = \frac{\Delta\lambda}{\sqrt{3}} \quad nm \tag{6}$$

This contribution acts on the spectral integral defining $y_i$ in Eq. (1) and propagates through the measurement, ultimately yielding an uncertainty referred to the reading. Differentiating Eq. (3) with respect to $\lambda_i$,

$$\frac{\partial \hat{R}_i(\lambda)}{\partial \lambda_i} = \frac{\lambda - \lambda_i}{\sigma_i^2}\,\hat{R}_i(\lambda), \tag{7}$$

and substituting in Eq. (1) gives the sensitivity of the reading to the filter centre,

$$\frac{\partial y_i}{\partial \lambda_i} = \int_\Lambda S(\lambda)\,\frac{\partial \hat{R}_i(\lambda)}{\partial \lambda_i}\,d\lambda = \int_\Lambda S(\lambda)\,\frac{\lambda - \lambda_i}{\sigma_i^2}\,\hat{R}_i(\lambda)\,d\lambda. \tag{8}$$

The integrand is odd about $\lambda_i$ weighted by $S(\lambda)$: Eq. (8) therefore vanishes for a perfectly flat source and grows where the source presents a steep spectral gradient across the passband. The corresponding uncertainty on the reading is

$$u_\lambda(y_i) = \left|\frac{\partial y_i}{\partial \lambda_i}\right| u(\lambda_i) \quad \text{counts} \tag{9}$$

Equation (9) is source-dependent through the sensitivity coefficient $\partial y_i/\partial\lambda_i$, it is therefore not a fixed device figure but is evaluated for each source in Section 3.1, where it is computed for the illuminant used in the reconstruction experiments of Besozzi et al.

As discussed above, the Gaussian model of Eq. (3) is only an approximation, and the true channel responsivities deviate from it. Figure 2 illustrates this for the AS7343, whose datasheet responsivities exhibit visible asymmetries, long tails, and side lobes with respect to the corresponding Gaussian fits. This responsivity mismatch introduces an additional uncertainty in the channel response, which is difficult to characterise for two reasons. First, the deviation is strongly device-dependent, and the datasheet curve only represents a nominal unit rather than the specific sensor in use. Second, since the channel reading is a spectral integral (Eq. 1), pointwise deviations in the line shape tend to partially cancel under integration; therefore, their effect has more impact on the spectral reconstruction problem, where the responsivity enters directly as a row of the measurement matrix $\mathbf{A}$ in Eq. (2), while it is less relevant to the reading $y_i$, where we are more interested in the absolute power rather than its distribution.

For these reasons, we quantify this contribution as the relative discrepancy between the integrated datasheet responsivity and the integrated Gaussian fit,

$$\delta_i = \frac{\left| \int_{\lambda_{\min}}^{\lambda_{\max}} \hat{R}_{i,\mathrm{ds}}(\lambda)\, d\lambda - \int_{\lambda_{\min}}^{\lambda_{\max}} \hat{R}_{i,\mathrm{gauss}}(\lambda)\, d\lambda \right|}{\int_{\lambda_{\min}}^{\lambda_{\max}} \hat{R}_{i,\mathrm{gauss}}(\lambda)\, d\lambda}, \tag{10}$$

where $\hat{R}_{i,\mathrm{ds}}(\lambda)$ is the responsivity curve reported in the datasheet and $\hat{R}_{i,\mathrm{gauss}}(\lambda)$ is the corresponding Gaussian fit of Eq. (3). Assuming a rectangular distribution over $[-\delta_i, +\delta_i]$, the associated standard uncertainty on the channel reading is

$$u_{R_i}(y_i) = \frac{\delta_i}{\sqrt{3}}\, y_i \quad \text{counts} \tag{11}$$

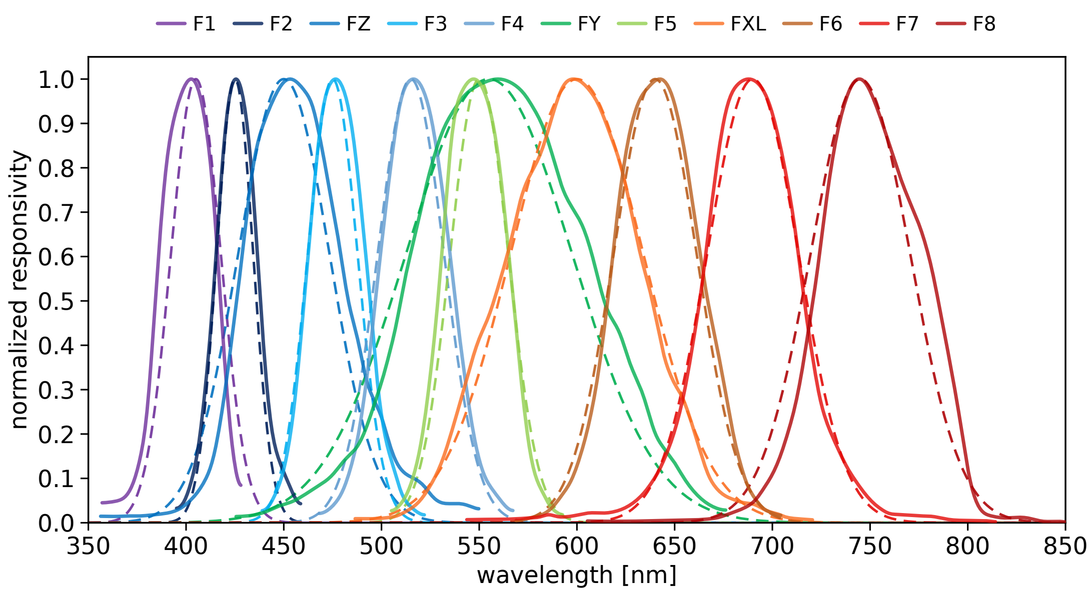


Figure 2. Datasheet responsivity curves of the AS7343 channels (solid) and their best-fit Gaussian profiles (dashed). The deviation between the two illustrates the responsivity uncertainty described in Section 2.2.

Since both contributions stem from the filter characteristics, they can be mitigated through a per-channel spectral calibration. Measuring the actual responsivity $\hat{R}_i(\lambda)$ with a tunable monochromator, as in Rodriguez et al.,[14] replaces the nominal centre wavelength and Gaussian profile with the true ones, suppressing both the centre-wavelength tolerance and the line-shape deviation. Performed against high-quality reference instrumentation, such a procedure could reduce these terms substantially, close to zero, at the cost of an individual characterisation of each device.

### 2.2.2 PGA uncertainty

The PGA stage applies an analog multiplicative factor $G$, selected via the AGAIN register, that scales the photocurrent. The manufacturer specifies, for each AGAIN setting, the minimum, typical, and maximum gain, normalised to the 64× setting; these values are reported in Table 1. The relative tolerance on $G$, taken as the half-range about the typical value, $\Delta G/G = (G_{\max} - G_{\min})/(2G_{\mathrm{typ}})$, can be represented under a rectangular distribution assumption, and therefore the standard uncertainty on the gain factor is

$$\frac{u(G)}{G} = \frac{\Delta G/G}{\sqrt{3}}. \tag{12}$$

Table 1. Gain tolerances declared in the AS7343 datasheet. Actual gains are normalised to the 64× setting ($G_{\mathrm{typ}} = 1$ by construction). The last column gives the relative tolerance $\Delta G/G = (G_{\max} - G_{\min})/(2G_{\mathrm{typ}})$.

| **AGAIN** | $G_{\min}$ | $G_{\mathrm{typ}}$ | $G_{\max}$ | $\Delta G/G$ (%) |
|---|---|---|---|---|
| 0.5× | 0.00749 | 0.00790 | 0.00828 | 5.0 % |
| 1× | 0.0150 | 0.0158 | 0.0165 | 4.7 % |
| 2× | 0.0300 | 0.0316 | 0.0332 | 5.1 % |
| 4× | 0.0610 | 0.0640 | 0.0670 | 4.7 % |
| 8× | 0.117 | 0.124 | 0.130 | 5.2 % |
| 16× | 0.235 | 0.247 | 0.259 | 4.9 % |
| 32× | 0.475 | 0.500 | 0.525 | 5.0 % |
| 64× | – | 1.000 | – | ref. |
| 128× | 1.90 | 2.00 | 2.10 | 5.0 % |
| 256× | 3.90 | 4.10 | 4.30 | 4.9 % |
| 512× | 8.10 | 8.60 | 9.10 | 5.8 % |
| 1024× | 15.2 | 16.9 | 18.6 | 10.1 % |
| 2048× | 28.2 | 34.75 | 41.3 | 18.8 % |

The relative tolerance is close to 5 % across most settings and degrades at the two highest gains, reaching about 19 % at 2048×. As discussed in Section 2.3, the treatment of the gain uncertainty depends on the calibration strategy. If a single calibration is reused across several gain settings (the reading being rescaled by the ratio of the nominal gains), a deviation $\Delta G$ between the true and the nominal gain induces the same relative deviation on the reading, so that

$$u_G(y_i) = y_i \, \frac{u(G)}{G} \quad \text{counts} \qquad \text{(shared calibration)}. \tag{13}$$

If, on the other hand, a separate calibration (Eq. 4) is performed at each gain setting, as in the procedure adopted in Besozzi et al.,[12] the actual gain, possibly perturbed by $u(G)$, is absorbed into the calibration coefficients $\{a_i, b_i\}$, the normalisation by $G$ is unnecessary, and the gain uncertainty does not propagate:

$$u_G(y_i) \equiv 0 \quad \text{counts} \qquad \text{(per-gain calibration)}. \tag{14}$$

### 2.2.3 ADC uncertainty

Modelling the reading as uniformly distributed over one quantisation step gives, in the count domain, the source-independent contribution

$$u_q(y_i) = \frac{1}{\sqrt{12}} \quad \text{counts}, \tag{15}$$

i.e. one half-LSB standard uncertainty, which sets a hard lower bound on the resolvable increment of the reading. Like the other count-domain terms, it is mapped to irradiance through the calibration in Section 2.3, where one step corresponds to an irradiance increment $1/D_i$ at the operating point.

The sensor datasheets further specify a residual noise on the digital reading of approximately 0.05 % of the full-scale value, representing one standard deviation:

$$u_n(y_i) \approx 5 \times 10^{-4}\, y_{\mathrm{FS}} \quad \text{counts}. \tag{16}$$

### 2.3 Uncertainty propagation

All the Type B sources identified above ($u_\lambda$, $u_{R_i}$, $u_G$, $u_n$ and $u_q$) are expressed in digital counts. Being mutually independent, they are first combined in the count domain into a single reading uncertainty,

$$u^2(y_i) = u_\lambda^2(y_i) + u_{R_i}^2(y_i) + u_G^2(y_i) + u_n^2(y_i) + u_q^2(y_i), \tag{17}$$

with $u_G$ taken from Eq. (14) or (13) according to the calibration strategy and $u_q = 1/\sqrt{12}$ from Eq. (15). This count-domain budget is a figure for the bare, uncalibrated device. To express the result in physical units, the reading is then converted to irradiance once, by inverting the quadratic calibration of Eq. (4),

$$E_i = \frac{-b_i + \sqrt{b_i^2 + 4\, a_i\, y_i}}{2\, a_i}. \tag{18}$$

The coefficients $\{a_i, b_i\}$ were estimated, in Besozzi et al.,[12] by a least-squares fit that also returns their standard uncertainties $u(a_i)$, $u(b_i)$ and covariance $\mathrm{cov}(a_i, b_i)$; the irradiance is therefore a function of three uncertain quantities, $E_i = E_i(y_i, a_i, b_i)$, all of which propagate to $u(E_i)$. Differentiating Eq. (18) implicitly from $y_i = a_i E_i^2 + b_i E_i$ gives the sensitivity coefficients

$$\frac{\partial E_i}{\partial y_i} = \frac{1}{D_i}, \qquad \frac{\partial E_i}{\partial a_i} = -\frac{E_i^2}{D_i}, \qquad \frac{\partial E_i}{\partial b_i} = -\frac{E_i}{D_i}, \qquad D_i \equiv 2a_i E_i + b_i = \sqrt{b_i^2 + 4a_i y_i}, \tag{19}$$

where $D_i$ is the local slope of the calibration curve. The combined reading uncertainty of Eq. (17) is mapped to irradiance through $\partial E_i/\partial y_i$,

$$u_y(E_i) = \frac{u(y_i)}{D_i}, \tag{20}$$

while the calibration coefficients add a further, source-independent term obtained from the remaining two sensitivities,

$$u_{\mathrm{cal}}^2(E_i) = \frac{E_i^4\, u^2(a_i) + E_i^2\, u^2(b_i) + 2\, E_i^3\, \mathrm{cov}(a_i, b_i)}{D_i^2}. \tag{21}$$

The covariance contribution is in general non-negligible, since the two fit coefficients are strongly anticorrelated, which makes $\mathrm{cov}(a_i, b_i) < 0$ and therefore reduces $u_{\mathrm{cal}}$.

Assuming the reading and the calibration contributions mutually independent, the combined Type B irradiance uncertainty on the $i$-th channel is

$$u^2(E_i) = \underbrace{\frac{u^2(y_i)}{D_i^2}}_{\text{reading}} + \underbrace{u_{\mathrm{cal}}^2(E_i)}_{\text{calibration}}. \tag{22}$$

Equation (22) defines the metrological floor of the device at the chosen operating point; its numerical evaluation for the AS7343 at ($t_{\mathrm{int}} = 200\,\mathrm{ms}$, $G = 64\times$) is reported in Section 3.1.

### 2.4 Effective number of independent measurements

While the matrix $\mathbf{C}$ provides a complete description of pairwise redundancies, a scalar summary of the overall channel independence is useful for inter-device comparison. We adopt the participation ratio of the eigenvalues of $\mathbf{C}$, a quantity widely used in random matrix theory and in the analysis of localisation phenomena, where it quantifies the effective number of modes contributing to a state. Denoting by $\{\mu_k\}_{k=1}^{M}$ the eigenvalues of $\mathbf{C}$, the participation ratio reads

$$M_{\text{eff}} = \frac{(\sum_k \mu_k)^2}{\sum_k \mu_k^2} = \frac{(\operatorname{tr}\mathbf{C})^2}{\operatorname{tr}(\mathbf{C}^2)} = \frac{M^2}{\sum_{i,j} C_{ij}^2}, \tag{23}$$

where the last equality follows from $\operatorname{tr}\mathbf{C} = M$ (unit diagonal) and $\operatorname{tr}(\mathbf{C}^2) = \sum_{i,j} C_{ij}^2$ (Frobenius norm). If the responsivities are mutually orthogonal, $\mathbf{C} = \mathbf{I}_M$, all eigenvalues equal one, and $M_{\text{eff}} = M$, which means that every channel contributes a fully independent piece of information, while for intermediate configurations, $1 \le M_{\text{eff}} \le M$. $M_{\text{eff}}$ counts not only how many eigenvalues are strictly non-zero, but also how concentrated the spectrum of $\mathbf{C}$ is. Two devices with the same nominal $M$ but different eigenvalue concentrations will yield different $M_{\text{eff}}$, capturing precisely the design-level differences that channel count alone overlooks.

### 2.5 Comparison with experimental reconstruction

The metrological framework introduced above characterises the sensors from a purely design-level standpoint: every quantity is computed from datasheet parameters and from the per-channel calibration coefficients alone, without any additional measurement. To assess its predictive value, and to also account for the centre-wavelength contribution $u_\lambda(E_i)$, the propagated irradiance uncertainty $u(E_i)$ of Eq. (22) is compared in Section 3.3 against the experimental spectral reconstruction reported in our previous calibration study,[12] in which the same two sensors were illuminated by a xenon arc lamp and their channel readings were inverted to estimate the source SPD. The Type B budget of Eq. (22) bounds the accuracy of the individual channel readings, but it does not capture a second limitation that is specific to the reconstruction problem and rooted in the channel layout itself: because the $M$ responsivities span only an $M$-dimensional subspace of $L^2(\Lambda)$, any spectral component lying outside that subspace is intrinsically unmeasurable and cannot be recovered by any inversion of Eq. (2). We quantify this through a spectral sampling uncertainty

$$u_s(\lambda) = 1 - [\mathbf{P}]_{\lambda\lambda}\,, \qquad \mathbf{P} = \mathbf{A}^\top \left(\mathbf{A}\mathbf{A}^\top\right)^+ \mathbf{A}, \tag{24}$$

where $\mathbf{P}$ is the orthogonal projector onto the subspace spanned by the channel responsivities and $[\mathbf{P}]_{\lambda\lambda} \in [0,1]$ is the fraction of a unit spectral feature localised at $\lambda$ that the channels can represent. Its complement $u_s(\lambda)$ is the unrepresentable fraction: it vanishes at the channel centres and rises in the inter-channel gaps, where the spectrum is effectively unsampled, and it is therefore largest for sensors whose passbands are widely spaced relative to their bandwidth. Being defined entirely by the placement and width of the channels, $u_s(\lambda)$ is a fixed property of the device and does not depend on the source; the pseudo-inverse $\left(\mathbf{A}\mathbf{A}^\top\right)^+$ keeps $\mathbf{P}$ well defined even when strong inter-channel overlap makes $\mathbf{A}\mathbf{A}^\top$ nearly singular. Unlike the instrumental terms, $u_s$ contributes nothing to the reading $y_i$: it acts only in the reconstruction, where it bounds the recoverable detail between channels.

## 3. RESULTS

### 3.1 Measurement uncertainty of the AS7343

The uncertainty budget is evaluated in three scenarios of increasing calibration effort: the bare *off-the-shelf* device, characterised only by datasheet parameters and digital readings; an *absolute* calibration following Besozzi et al.,[12] which maps the readings to irradiance through the quadratic curve of Eq. (4); and a *spectral* calibration following Rodriguez et al.,[14] which additionally measures the true channel responsivity. Throughout this section the centre-wavelength term $u_\lambda$ is left out of the budget, since it is source-dependent (Eq. 9) and is evaluated for the xenon illuminant in Section 3.3. All relative terms are referred to the full-scale reading $y_{\text{FS}} = 65535$, which gives the worst-case figure.

Table 2. Per-channel responsivity deviation $\delta_i$ of the AS7343, obtained from Eq. (10) as the relative discrepancy between the integrated datasheet responsivity and its Gaussian fit.

| **Channel** | $\int \hat{R}_{\mathrm{ds}}$ [nm] | $\int \hat{R}_{\mathrm{gauss}}$ [nm] | $\delta_i$ | $\delta_i$ [%] |
|---|---|---|---|---|
| F1 | 34.30 | 31.93 | 0.0740 | 7.40 |
| F2 | 26.86 | 23.42 | 0.1470 | 14.70 |
| FZ | 63.67 | 58.55 | 0.0875 | 8.75 |
| F3 | 35.60 | 31.93 | 0.1147 | 11.47 |
| F4 | 43.07 | 42.58 | 0.0116 | 1.16 |
| FY | 110.48 | 106.45 | 0.0379 | 3.79 |
| F5 | 40.48 | 37.26 | 0.0866 | 8.66 |
| FXL | 85.60 | 85.16 | 0.0052 | 0.52 |
| F6 | 54.54 | 53.22 | 0.0248 | 2.48 |
| F7 | 60.74 | 58.55 | 0.0374 | 3.74 |
| F8 | 64.06 | 63.87 | 0.0030 | 0.30 |

### 3.1.1 Off-the-shelf uncertainty

Without any calibration, the only available information is the digital reading and the nominal datasheet parameters, so the budget is assembled directly in counts. The responsivity deviation $\delta_i$ of Eq. (10) is first evaluated and reported in Table 2, spanning from 0.30 % (F8) to 14.70 % (F2).

Taking F5 as the representative channel ($\delta_{F5} = 0.0866$), the responsivity-deviation term follows Eq. (11),

$$u_{R_i}(y_{\mathrm{FS}}) = \frac{\delta_{F5}}{\sqrt{3}}\, y_{\mathrm{FS}} = 0.050 \cdot 65535 \approx 3277 \text{ counts.} \tag{25}$$

Since the device is operated without calibration, the gain tolerance propagates according to Eq. (13); adopting the representative tolerance $\Delta G/G \simeq 5\,\%$ of Table 1 gives $u(G)/G = 2.9\,\%$ and $u_G(y_{\mathrm{FS}}) \approx 1892$ counts. The ADC noise of Eq. (16) amounts to $u_n = 5 \times 10^{-4}\, y_{\mathrm{FS}} \approx 33$ counts, while the quantisation reduces, in the count domain, to one $1/\sqrt{12}$-LSB uniform interval, $u_q \approx 0.29$ counts. The resulting budget is collected in Table 3.

Table 3. Off-the-shelf Type B uncertainty budget for channel F5 of the AS7343, expressed in digital counts and referred to full scale $y_{\mathrm{FS}} = 65535$. The centre-wavelength term is excluded (source-dependent, Section 3.3).

| **Source** | **Symbol** | $u(y_i)$ [counts] |
|---|---|---|
| Responsivity deviation | $u_{R_i}$ | 3277 |
| PGA gain | $u_G$ | 1892 |
| ADC noise | $u_n$ | 33 |
| ADC quantisation | $u_q$ | 0.29 |
| **Combined** | $u(y_i)$ | 3784 |

Combining the terms in quadrature yields $u(y_i) \approx 3784$ counts, i.e. about 5.8 % of full scale, dominated by the responsivity deviation and, secondarily, by the gain tolerance; the two ADC contributions are negligible by comparison.

### 3.1.2 Absolute calibration uncertainty

Applying the calibration of Besozzi et al.[12] maps the count-domain budget to irradiance. Figure 3 shows the quadratic curve of channel F5 at the operating point ($t_{\mathrm{int}} = 200\,\mathrm{ms}$, $G = 64\times$), with coefficients $a_{F5} = 0.413$ and $b_{F5} = 82.4$ (relative uncertainties $u(a)/a = 7.0\,\%$, $u(b)/b = 3.1\,\%$ from the fit confidence intervals) and full-scale irradiance $E_{\mathrm{FS},ch5} = 311\,\mu W/cm^2$. The reading is converted once through the tangent slope

$D_{F5} = \sqrt{b_{F5}^2 + 4a_{F5}y_{\mathrm{FS}}} = 339$ (Eq. 19), so that one count maps to $1/D_{F5} = 2.95 \times 10^{-3}\,\mu W/cm^2$. The fit confidence intervals further contribute the calibration term of Eq. (21), $u_{\mathrm{cal}} = 8.57\,\mu W/cm^2$, evaluated here with $\mathrm{cov}(a,b) = 0$ as a conservative upper bound.

The gain term depends on the calibration strategy (Section 2.3). If a dedicated curve is acquired at each gain setting (*per-gain* calibration), the gain is absorbed into the coefficients $\{a_i, b_i\}$ and $u_G \equiv 0$ (Eq. 14). If a single curve is instead reused across gains (*shared* calibration), the gain tolerance propagates and, with $u(G)/G = 2.9\,\%$, contributes $u_G(E_i) = 5.58\,\mu W/cm^2$. Both cases are reported in Table 4.

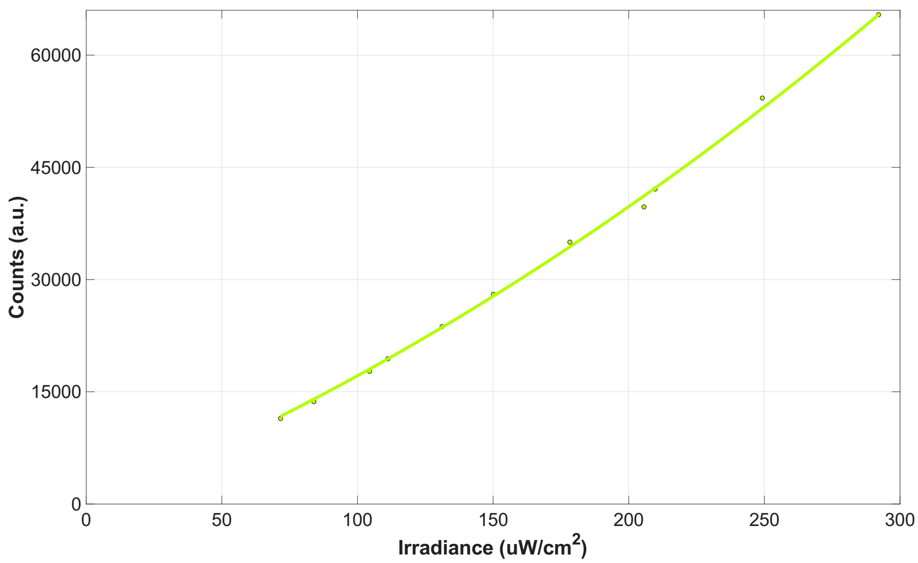


Figure 3. Quadratic calibration curve $y_i = a_i E_i^2 + b_i E_i$ for the representative channel ($ch_5$) of the AS7343 at ($t_{\mathrm{int}} = 200\,\mathrm{ms}$, $G = 64\times$)

### 3.1.3 Spectral calibration uncertainty

A per-channel spectral calibration with a tunable monochromator, as in Rodriguez et al.,[14] measures the actual responsivity $\hat{R}_i(\lambda)$ and replaces the nominal centre wavelength and Gaussian profile with the true ones. This suppresses both filter-related contributions ($u_{R_i} = 0$, $u_\lambda = 0$) and, being performed channel by channel at a known gain, also removes the gain tolerance ($u_G = 0$). The residual budget then reduces to the ADC terms alone, as reported in the last column of Table 4.

In the per-gain absolute calibration the combined uncertainty is $u(E_i) = 12.9\,\mu W/cm^2$, shared almost equally between the responsivity deviation ($9.67\,\mu W/cm^2$) and the calibration coefficients ($8.57\,\mu W/cm^2$); the ADC terms are two to four orders of magnitude smaller. Reusing a single calibration across gains adds the gain tolerance and raises the combined value to $14.1\,\mu W/cm^2$, confirming that per-gain calibration is preferable whenever the gain is changed during acquisition. The spectral calibration removes both filter-related terms, after which the residual uncertainty is dominated by the calibration coefficients, $u(E_i) \approx 8.6\,\mu W/cm^2$; further improvement would require reducing the uncertainty of the absolute calibration itself.

## 3.2 Nominal figures of merit

As noted earlier, two commercially available spectral sensors have been evaluated for their nominal performance by computing the crosstalk matrices and the effective number of channels. The crosstalk matrices in Figure 4 highlight two qualitatively different design strategies. The AS7341 emerges as more balanced, since its filters are evenly spaced across the visible range and have homogeneous bandwidths, yielding adjacent-pair crosstalks confined within [0.20, 0.34]. The result is the highest efficiency ($M_{\mathrm{eff}}/M = 0.88$) despite having fewer channels than the AS7343, which suffers from the broad FWHM of its FY and FXL channels, producing strong overlaps

Table 4. Type B irradiance uncertainty for channel F5 of the AS7343 at ($t_{\text{int}} = 200\,\text{ms}$, $G = 64\times$), $E_{\text{FS},ch5} = 311\,\mu W/cm^2$. Reading-domain terms are mapped through the tangent slope $1/D_{F5}$; the calibration term $u_{\text{cal}}$ propagates the fit confidence intervals of $a_{F5}, b_{F5}$ from Besozzi et al.[12] Columns: absolute calibration with per-gain ($u_G = 0$) and shared ($u_G \neq 0$) strategy; spectral calibration,[14] which removes the filter terms. The centre-wavelength term is source-dependent (Section 3.3).

| **Source** | **Symbol** | absolute per-gain | absolute shared | spectral (Rodriguez) |
|---|---|---|---|---|
| Centre wavelength | $u_\lambda$ | source-dep. | source-dep. | 0 |
| Responsivity deviation | $u_{R_i}$ | 9.67 | 9.67 | 0 |
| PGA gain | $u_G$ | 0 | 5.58 | 0 |
| ADC noise | $u_n$ | 0.097 | 0.097 | 0.097 |
| ADC quantisation | $u_q$ | 0.00085 | 0.00085 | 0.00085 |
| Calibration $(a, b)$ | $u_{\text{cal}}$ | 8.57 | 8.57 | 8.57 |
| **Combined** $[\mu W/cm^2]$ | $u(E_i)$ | 12.9 | 14.1 | 8.57 |

with their neighbours (up to $C_{i,i+1} = 0.78$), while also offering the widest spectral coverage and the largest channel count. As a consequence, its $M_{\text{eff}}$ collapses to 7.05, essentially identical to that of the AS7341 despite three additional nominal channels. This is a clear-cut demonstration that channel count alone is a poor predictor of metrological quality, since the two devices share the same number of independent measurements.

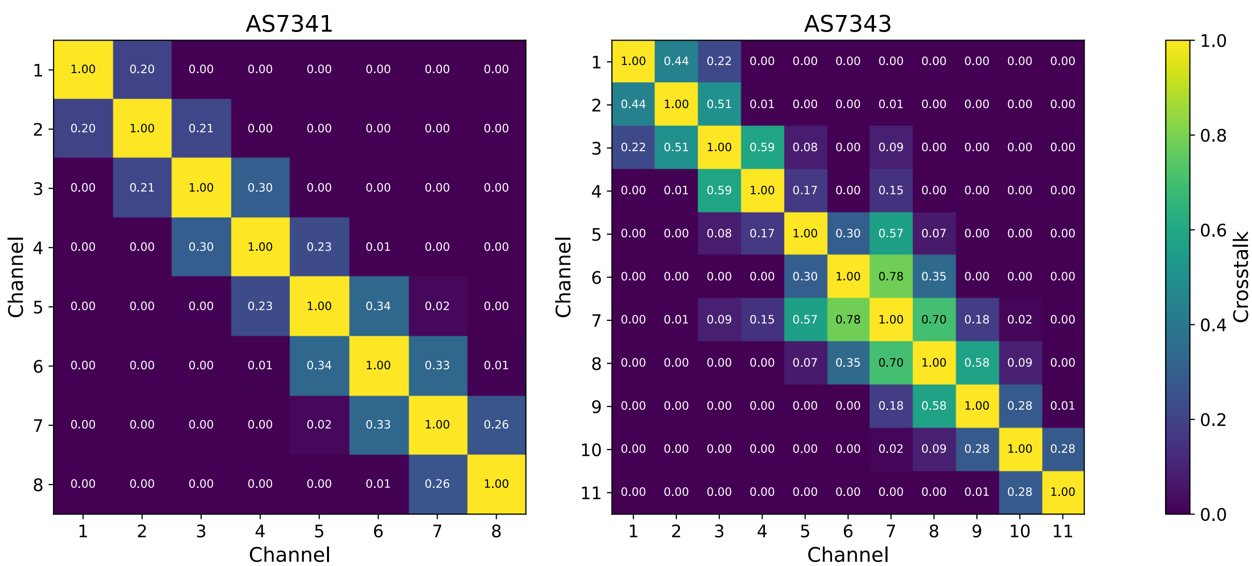


Figure 4. Crosstalk matrices **C** for the AS7341 ($M = 8$, left), and AS7343 ($M = 11$, right). Off-diagonal magnitude directly reflects the loss of independence between channel pairs.

### 3.3 Comparison with experimental spectral reconstruction

The figures of merit and the AS7343 irradiance uncertainty computed above characterise the sensors from a purely design-level standpoint. To assess their predictive value, we compare them against the experimental reconstruction errors measured in our previous calibration study[12] for the AS7341 and AS7343, illuminated by a Xenon arc lamp reference source. The ground-truth SPDs were measured with a calibrated dispersive spectrometer.

For each sensor, Figure 5 reports the reference SPD, the reconstructed SPD and its $\pm 1\sigma$ band. The xenon

Table 5. Metrological figures of merit from nominal datasheet values, computed for the two sensors. $C_{i,i+1}$ is the [min, max] range over adjacent pairs.

| **Sensor** | $M$ | **Range (nm)** | $C_{i,i+1}$ | $M_{\text{eff}}$ |
|---|---|---|---|---|
| AS7341 | 8 | 402–706 | [0.20, 0.34] | 7.07 |
| AS7343 | 11 | 390–775 | [0.17, 0.78] | 7.05 |

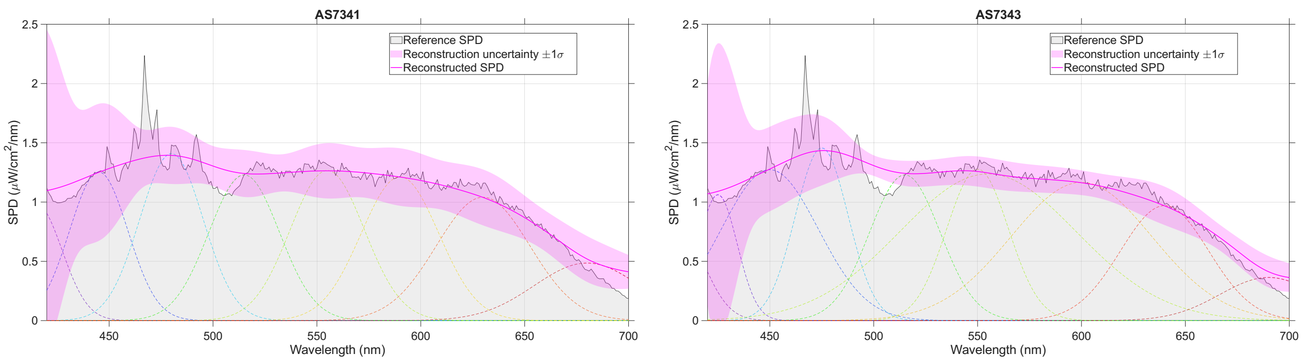


Figure 5. Experimental reconstruction for the xenon illuminant from,[12] for the AS7341 (left) and AS7343 (right). Each panel shows the reference SPD, the reconstructed SPD and its $\pm 1\sigma$ uncertainty band.

source is the most demanding of the set: a smooth continuum overlaid with dense, sharp emission lines whose width is far below the channel passbands. In both devices the reconstructed SPD tracks the broad continuum well but smooths the emission lines into the envelope, leaving them as unresolved residuals of the reference curve. This is the regime in which the spectral sampling uncertainty $u_s$ of Eq. (24) dominates: the line content falls almost entirely in the inter-channel gaps and is therefore unrecoverable by any inversion, irrespective of the instrumental floor.

The $\pm 1\sigma$ band is markedly wider at the blue end (420–490 nm), where the brightest xenon lines cluster and where, for the AS7343, the F2 and F3 channels deviate most strongly from the Gaussian model (Table 2). The blue-end band of the AS7343 is visibly larger than that of the AS7341, consistent with both the stronger non-Gaussian behaviour of its blue channels and the strong overlap of its broad FY and FXL filters ($C_{i,i+1} = 0.78$). Away from the blue edge the two reconstructions are comparable, confirming that the additional AS7343 channels add little usable information on this source. The comparable performance of the two devices, despite the three extra nominal channels of the AS7343, is the experimental counterpart of their near-identical effective channel count ($M_{\text{eff}} = 7.05$ versus 7.07, Table 5).

## 4. CONCLUSIONS

We have presented a metrological framework that characterises compact multi-channel spectral sensors from their datasheet specifications and per-channel calibration coefficients alone. The framework couples a GUM-compliant Type B uncertainty budget with two design-level figures of merit, the inter-channel crosstalk matrix $\mathbf{C}$ and the effective number of independent measurements $M_{\text{eff}}$, and was applied to two ams osram devices, the AS7341 and the AS7343.

The uncertainty analysis developed in detail for the AS7343 shows that, off-the-shelf, the combined standard uncertainty reaches about 5.8 % of full scale, dominated by the responsivity line-shape deviation and, secondarily, by the PGA gain tolerance. An absolute calibration maps this floor to irradiance, where the responsivity deviation ($9.67\,\mu W/cm^2$ for the representative channel F5) and the uncertainty of the calibration coefficients ($8.57\,\mu W/cm^2$) become the two leading terms, for a combined $12.9\,\mu W/cm^2$; a dedicated per-gain calibration is preferable to a single shared curve whenever the gain is changed during acquisition. A full spectral calibration with a tunable monochromator removes both filter-related contributions, leaving the calibration-coefficient uncertainty as the residual floor (about $8.6\,\mu W/cm^2$), at the cost of an individual characterisation of each device.

The figures of merit convey the central message of this work. Although the AS7343 offers three additional nominal channels and the widest spectral coverage, the strong overlap of its broad FY and FXL filters (adjacent crosstalk up to 0.78) reduces its effective channel count to $M_{\text{eff}} = 7.05$, essentially identical to the 7.07 of the more uniformly spaced AS7341. Channel count alone is therefore a poor predictor of metrological quality.

This conclusion is borne out by the experimental spectral reconstruction of our previous study. On the xenon source, whose dense emission lines are far narrower than the channel passbands, both sensors reproduce the broad continuum but smooth the sharp lines into the envelope; the residual uncertainty is governed by the spectral-sampling term $u_s$, as the line content falls in the unrepresentable inter-channel gaps. The two devices perform comparably, with the AS7343 showing a larger reconstruction uncertainty only at the blue end, where its F2 and F3 channels depart most from the Gaussian model. The extra AS7343 channels thus prove largely redundant, and where its crosstalk is locally strong they add no usable information. The agreement between datasheet-based prediction and measured reconstruction supports the proposed metrics as a practical, predictive tool for fair inter-device comparison and for informed sensor selection ahead of any experimental campaign.

## REFERENCES


1. Lebourgeois, V., Bégué, A., Labbé, S., Houlès, M., and Martiné, J. F., "A light-weight multi-spectral aerial imaging system for nitrogen crop monitoring," *Precision Agriculture* **13**, 525–541 (Oct. 2012).
2. Nguyen, T.-N., Pham, Q.-H., Nguyen, D.-K., Nguyen, H.-M., Le Ho, T.-L., Le, Q.-A., and Tran, N.-T., "Painless and accurate ai-driven method for personal glucose tracking based on multi-spectral sensing," in [*International Conference on Intelligent Systems and Data Science*], 133–146, Springer (2025).
3. Ren, D. D. W., Tripathi, S., and Li, L. K. B., "Low-cost multispectral imaging for remote sensing of lettuce health," *Journal of Applied Remote Sensing* **11**, 016006 (Jan. 2017).
4. Liu, G. and Ma, Z., "Study on a novel portable urine analyzer based on optical fiber bundles," *Measurement* **130**, 412–421 (2018).
5. Besozzi, A., Gibertoni, G., Rovati, L., and Gibaldi, A., "Development and testing of a Lightweight, All-Day Glasses-Mounted Wearable: Investigating the Visual Environment in Children for Myopia Risk Assessment," in [*Proceedings of the TC2 International Symposium on Photonics - PhotoMet 2025*], 42–43, IMEKO, Modena, ITALY (2025).
6. Gibaldi, A., Harb, E. N., Wildsoet, C. F., and Banks, M. S., "A child-friendly wearable device for quantifying environmental risk factors for myopia," *Translational Vision Science & Technology* **13**(10), 28–28 (2024).
7. Yang, Z., Albrow-Owen, T., Cai, W., and Hasan, T., "Miniaturization of optical spectrometers," *Science* **371**, eabe0722 (2021). DOI: 10.1126/science.abe0722.
8. Mousa, M. A., Rafat, N. H., and Saleh, A. A. E., "Angle-multiplexed metasurface-grating for ultra-compact spectrometers," *Optics Letters* **51**, 2128 (Apr. 2026).
9. Botero-Valencia, J. S., Castillo-Escudero, J., Alvarez-Lucena, L. D., and Restrepo-Arias, J., "Multi-channel low-cost light spectrum measurement using a multilayer perceptron," *Energy and Buildings* **199**, 579–588 (July 2019).
10. ams OSRAM, *AS7341: 11-Channel Spectral / Color Sensor (Datasheet)* (2020). Document DS000504 (or latest revision).
11. ams OSRAM, *AS7343: 14-Channel Spectral / Color Sensor (Datasheet)* (2023). Document DS000673 (or latest revision).
12. Besozzi, A., Gibertoni, G., Gibaldi, A., and Rovati, L., "Flexible calibration method: photometric and radiometric measurements with compact low-cost multi-channel sensors," *Acta IMEKO* (2026).
13. JCGM, "Evaluation of measurement data - Guide to the expression of uncertainty in measurement (GUM)," Tech. Rep. JCGM 100:2008, BIPM (2008).
14. Rodriguez, D., Ribas, J., Quintana-Barcia, P., Gacio, D., Mallada, D., and Perdigao, M. S., "m-edi measurement using low-cost spectrometric sensors based on photodiode arrays with narrowband color filters: An exploration of alternative calibration methods," *Sensors* **25**(23) (2025).